PCCP

PAPER

Cite this: *Phys. Chem. Chem. Phys.*, 2017, **19**, 30616

A direct dynamics study of the deprotonated guanine·cytosine base pair: intra-base pair proton transfer, thermal dissociation *vs.* collision-induced dissociation, and comparison with experiment†

Jianbo Liu

Direct dynamics trajectories were calculated at the B3LYP/6-31G* level of theory to examine the intra-base pair proton transfer and dissociation of the deprotonated guanine (G)·cytosine (C) base pair under different excitation conditions, and to explore the origin of the nonstatistical product branching reported in a collision-induced dissociation (CID) experiment (*Phys. Chem. Chem. Phys.* 2016, **18**, 32222). Trajectories for thermal excitation were initiated at two major conformers G·[C−H]$^-$ (hydrogen-bonded guanine and N1-deprotonated cytosine) and G·[C−H]$^-$_PT (formed by proton transfer from the N1 of guanine to the N3 of deprotonated cytosine), and at their transition state (TS). Thermal excitation was realized by sampling molecular vibrational levels and TS's reaction coordinate energy with Boltzmann distributions at temperatures of 960 and 1330 K, which correspond to classical energies of 3.0 and 5.0 eV, respectively. Thermally excited trajectories undergo intra-base pair proton transfer extensively. The resulting conformation scrambling leads to nearly equal branching between the dissociation channels of [G−H]$^-$ + C and G + [C−H]$^-$. Collisions of G·[C−H]$^-$ and G·[C−H]$^-$_PT with Ar were each simulated at collision energies of 3.0 and 5.0 eV, respectively. The probability for intra-base pair proton transfer decreases substantially in collision trajectories. The CID product branching calculated on the basis of the population-weighted trajectory results of G·[C−H]$^-$ and G·[C−H]$^-$_PT reveals a strong preference for [G−H]$^-$ + C, consistent with the experiment. Trajectory analysis corroborates that non-statistical CID is attributed to inadequate conformation interconversion during collisional activation, and to the faster dissociation of the G·[C−H]$^-$_PT conformer albeit G·[C−H]$^-$_PT has nearly the same translational-to-vibrational energy transfer as G·[C−H]$^-$.

Received 7th September 2017,
Accepted 24th October 2017

DOI: 10.1039/c7cp06124b

rsc.li/pccp

I. Introduction

The detrimental effects of ionizing radiation on DNA start with channeling the radiation energy deposited in cells into the production of low-energy electrons, followed by the capture of electrons by DNA and the subsequent decay of transient anions localized on the DNA's components[1]—the so-called dissociative electron attachment (DEA). Taking the isolated cytosine (C) nucleobase as an example, accommodation of an extra electron into an unoccupied π* molecular orbital leads to the formation of a transient negative ion C*$^-$. C*$^-$ subsequently decomposes by ejecting a neutral hydrogen atom at the N1 position that would normally form a link to the sugar-phosphate backbone in the double-helical form of DNA,[2,3] leading to the formation of N1-deprotonated cytosine [C–H]$^-$. When DEA and the ensuing dehydrogenation of nucleobases occur within the DNA network, it induces a cascade of events including changing the reactivity of DNA nucleobases towards reactive oxygen species,[4] single- and double-strand breaks,[1] and mispairing of complementary bases.[5,6] Of relevance to these processes is that the deprotonation of C prompts proton transfer (PT) within guanine·cytosine (G·C) base pairs.[7] Intra-base pair PT relocates charge within G·C and introduces structural and energetic perturbations. Therefore, understanding the dynamics of intra-base pair PT and the most probable structure of deprotonated G·C is crucial to understanding the explicit molecular origin of ionizing radiation-induced biological sequelae.

Recently, we reported a collision-induced dissociation (CID) experiment of deprotonated G·C and 9-methylguanine·cytosine (9MG·C) base pairs,[7] with the aim of probing their structures and bond energies. The experiment was performed by colliding the base pair ions with rare gas, to avoid the complications

Department of Chemistry and Biochemistry, Queens College and the Graduate Center of the City University of New York, 65-30 Kissena Blvd., Queens, NY 11367, USA. E-mail: jianbo.liu@qc.cuny.edu; Tel: +1-718-997-3271

† Electronic supplementary information (ESI) available: Computational details, and MPG movies for the trajectories shown in Fig. 3–5. See DOI: 10.1039/c7cp06124b

from chemistry or internal states of the collision gas. We measured CID cross sections as a function of collision energy (E_{col}) using guided-ion-beam tandem mass spectrometry. It turned out that the apparently simple collision systems proved to be complex. Most notably, the dissociation product branching ratios are 1–2 orders of magnitude different from that would be expected on the basis of the statistical analysis of reaction potential energy surfaces (PESs). Such findings have provided insight into the less intuitive aspect of base pair chemistry and have important biological implications, considering that lifetimes for isolated G·C base pairs are in the range of 7–40 ms (at 15 °C),[8] and base pair opening is a prerequisite for replication and transcription of double-stranded DNA, and for protein–nucleic acid recognition.[8,9]

Herein a quasi-classical trajectory (QCT) study was carried out for deprotonated G·C. The work was designed to assess the respective dynamics of deprotonated G·C upon thermal excitation and collisional activation, and to identify the origin of the nonstatistical base-pair opening kinetics in the experiment. The remainder of the article is organized as follows. Reaction coordinates for deprotonated G·C and 9MG·C and the CID experimental results are outlined in Section II. Approaches for dynamics simulations of thermal excitation and collisional activation are described in Section III, with detailed computational methodologies provided in the ESI.† Trajectory results are presented in Section IV, including the nature of trajectories, reaction pathways and probabilities, and the distributions of product translational (E_{trans}), vibrational (E_{vib}) and rotational (E_{rot}) energies. Finally, some conclusions are drawn in Section V.

II. Summary of reaction PESs and the CID experiment

Reaction PESs for deprotonated G·C and 9MG·C are summarized in Fig. 1. Guanine has two major tautomers 7HG and 9HG that differ in which of the N7 and N9 positions carries an H atom. The latter tautomer represents the correct guanine structure in nucleoside and DNA, and is shown in Fig. 1. PESs were calculated at the DFT, RI-MP2 and DLPNO-CCSD(T) levels of theory augmented with a range of basis sets.[7] The basis set superposition error was corrected for using counterpoise correction. Among the selected methods, B3LYP/aug-cc-pVQZ was found to be the most acceptable. Deprotonated 9HG·C and 9MG·C present identical PES profiles and energetics: (1) each base pair has two major conformations: the conventional one that retains the Watson–Crick H-bonding motif between neutral guanine (or 9MG) and N1-deprotonated cytosine $[C–H]^-$,[10] and the proton-transferred one that forms *via* proton transfer (PT) from guanine N1 to the N3 of $[C–H]^-$. For simplification, they are denoted as 9HG·$[C–H]^-$ (or 9MG·$[C–H]^-$) and 9HG·$[C–H]^-$_PT (or 9MG·$[C–H]^-$_PT), respectively; (2) the conventional and proton-transferred conformers are nearly isoenergetic and interconvert *via* a PT transition state (TS), resulting in a double-well PES; (3) the conventional conformer dissociates into 9HG (or 9MG) + $[C–H]^-$, whereas the proton-transferred conformer dissociates into deprotonated $[9HG–H]^-$ (or $[9MG–H]^-$) + neutral C, with the dissociation threshold energy being 0.02–0.05 eV higher than the former. There are no reverse activation barriers for dissociation asymptotes.

Experimental results for deprotonated G·C and 9MG·C in collisions with Xe are summarized in Fig. 2, which give the E_{col} (in the center-of-mass frame) dependence of CID product cross sections and branching ratios.[7] $[G–H]^-$/$[9MG–H]^-$ and $[C–H]^-$ were all detected in product ion mass spectra, indicating that the conventional and proton-transferred conformers co-exist in the gas phase. Dissociation threshold energies for individual channels, indicated by the arrows in Fig. 2a and b, were extracted by fitting the E_{col} dependence of product cross sections to the true $\sigma(E_{col})$ functions that were generalized from a modified line-of-center model[11,12] and convoluted with experimental energy broadening and kinetic shifts.[13] The agreement between the experimental fitting and the calculated dissociation thresholds validates the PESs shown in Fig. 1. On the basis

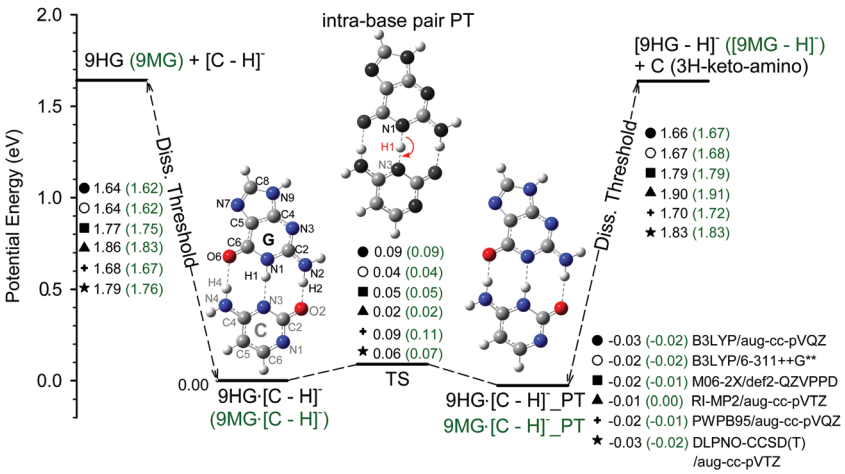

Fig. 1 Reaction coordinates for deprotonated G·C and 9MG·C. Numbering schemes for guanine and cytosine are presented. Energies were calculated at various levels of theory as indicated, including thermal corrections at 298 K. Data for deprotonated 9MG·C are indicated in parentheses.

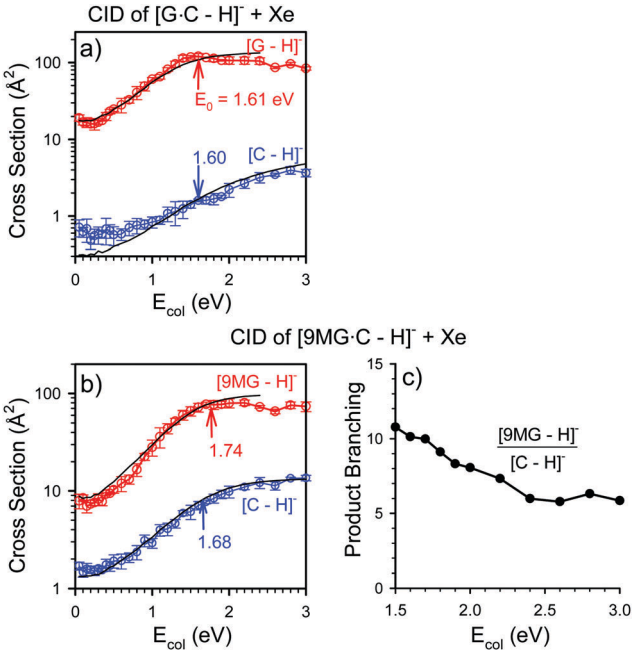

Fig. 2 CID product cross sections and branching ratios as a function of E_{col}. (a) $[G{\cdot}C{-}H]^-$ + Xe, and (b and c) $[9MG{\cdot}C{-}H]^-$ + Xe. Black plots in (a) and (b) are convoluted $\sigma(E_{col})$, with the fit dissociation thresholds indicated by arrows.

of the Rice–Ramsperger–Kassel–Marcus (RRKM)[14] modeling of the PESs, the interconversion between the conventional and proton-transferred conformers occurs at a rate of 10^{12} s^{-1} that is 7 orders of magnitude faster than the dissociation of the base pair. Therefore, a thermodynamical equilibrium could be assumed between the two activated conformers with the equilibrium constant being E_{col}-dependent. It follows that the dissociation of the ($9HG{\cdot}[C{-}H]^- \rightleftharpoons 9HG{\cdot}[C{-}H]^-$_PT) ensemble, if happened statically, would have produced a branching ratio of $\frac{[9HG{-}H]^- + C}{9HG + [C{-}H]^-} = \frac{1}{2.3}$ at E_{col} = 2.0 eV, slightly decreasing to $\frac{1}{2.7}$ at $E_{col} \geq 3.0$ eV. Similar product branching could be predicted for the statistical dissociation of the ($9MG{\cdot}[C{-}H]^- \rightleftharpoons 9MG{\cdot}[C{-}H]^-$_PT) ensemble; that is $\frac{[9MG{-}H]^- + C}{9MG + [C{-}H]^-} = \frac{1}{7.6}$ at 2.0 eV and $\frac{1}{3.8}$ at 3.0 eV. One surprise, therefore, was that the experimental CID products were overwhelmingly dominated by $[G{-}H]^-$ or $[9MG{-}H]^-$, as illustrated in Fig. 2.

A fact that has complicated the CID experiment of deprotonated G·C is that the guanine moiety comprises 38% of the 9HG tautomer and 62% of 7HG in the gas phase. The CID results of deprotonated G·C thus represent a population-weighted average of deprotonated 7HG·C and 9HG·C. The PES for deprotonated 7HG·C was reported elsewhere.[7] Here suffice it to say that the branching ratio of $\frac{[G{-}H]^- + C}{G + [C{-}H]^-}$ originating from CID of deprotonated 9HG·C should be close to that of $\frac{[9MG{-}H]^- + C}{9MG + [C{-}H]^-}$ measured from deprotonated 9MG·C (see Fig. 2c) in that 9MG has capped the N9 position and thus eliminated N9H–N7H tautomerization. The experimental ratio of $\frac{[9MG{-}H]^- + C}{9MG + [C{-}H]^-}$ reaches a maximum of $\frac{11}{1}$ at E_{col} = 1.5 eV, and levels off above 2.5 eV with a ratio near $\frac{6}{1}$. Experimental product branching ratios are therefore the opposite of the RRKM predictions. Failure of the RRKM modeling implies that the reactions of base pairs are significantly nonstatistical.

III. Approaches for dynamics simulations of excitation and dissociation of deprotonated G·C

There are three stages at which nonstatistical behavior may possibly evolve for the deprotonated base pairs. The first is at the TS for intra-base pair PT. The distance from G(N1) to C(N3) is shortened by 0.3 Å at the TS. To accommodate the decrease of rG(N1)–C(N3) and meanwhile maintain the three intra-base pair hydrogen bonds, the TS has to twist the dihedral angle G(C6–N1)–C(N3–C4) to 25°. This may bring about a dynamic bottleneck for conformation interconversion. The second stage deals with the dissociation of the base pair. Because there is no reverse barrier, a "loose" transition state[15] was assumed in the RRKM modeling of base pair dissociation.[7] However, the location of the dividing surface between the reactant and product regions of the phase space may actually vary with activation energy.[16] Finally, RRKM assumes that, regardless of initial excitation modes, rapid intramolecular vibrational energy redistribution (IVR) will create a random energy distribution on a time scale much shorter than unimolecular lifetime.[17] But it is not unlikely that CID may produce short-time nonstatistical fragmentation, as observed in a number of experiments[13,18] and dynamics simulations.[19–21] A representative example is the different dissociation pathways and probabilities following thermal excitation *vs.* collisional activation of a tripeptide reported by Hase and co-workers.[21]

To elucidate the aforementioned dynamics questions and the mechanism by which the CID product branching was determined, Born–Oppenheimer direct dynamics simulations were carried out. One advantage of direct dynamics simulations is that potential energy and its gradients needed to solve the classical equations of motions are calculated at each step "on the fly". Trajectories do not necessarily follow minimum-energy pathways, particularly at high energies. Instead, molecules explore multiple minima in a conformational landscape and a reaction PES, and show what the new reaction pathways could be. Three approaches were utilized in the present dynamics simulations. The first approach was to simulate the dissociation of randomly excited base pairs, where trajectories started at the conventional and proton-transferred conformers, respectively, and were excited to a high vibrational temperature of 960 K. The second approach was to follow the trajectories evolving from the TS connecting the conventional and proton-transferred structures and directed randomly towards either structure. Trajectories were propagated at two different activation temperatures (960 and 1330 K), to determine whether there is an inherent preference for a specific product channel as a result of dynamics effects. The last approach was to model activation and dissociation of

deprotonated base pairs in collisions with rare gas at E_{col} of 3.0 and 5.0 eV, respectively, with the purpose of determining whether the non-random excitation in collisions affects the ensuing dissociation dynamics and its energy dependence. Collision trajectories were simulated under the conditions mimicking the CID experiment,[7] except that, to maintain a reasonable computational cost, Xe was replaced by Ar as the collision gas. It has been observed in the CID of many systems that in the near threshold energy range Ar presents collision dynamics similar to Xe.[13]

As demonstrated in Fig. 1, deprotonated 9HG·C and 9MG·C have identical PT barriers and dissociation thresholds. Schlegel and co-workers have examined the effects of N9-substitution on guanine reactions, and found that those substituted at N9 with methyl, hydroxymethyl and methoxyethyl groups have similar reactivity as 9HG.[22] In light of these findings, the present simulations are focused only on deprotonated 9HG·C (referred to as deprotonated G·C in the following discussion).

Trajectories were calculated using VENUS 99 of Hase *et al.*[23,24] to set up initial conditions, and the Hessian-based predictor-corrector algorithm[25] implemented in Gaussian 09[26] to integrate trajectories, with Hessians recalculated every 5 steps. The B3LYP/6-31G* level of theory was used as it represented a good compromise between computational demand and chemistry accuracy. Trajectories of representative collisions were recalculated at B3LYP/6-31G** to test how a basis set with the explicit polarization term for hydrogen atoms would affect trajectory outcomes. It was found that B3LYP/6-31G** reproduced the proton transfer and collision dynamics observed at B3LYP/6-31G*. Trajectories were propagated with a step size of 0.25 amu$^{1/2}$ Bohr ($\sim$0.5 fs). A quadratically convergent SCF procedure[27] was used (*i.e.* SCF = XQC) in case the first-order SCF failed to converge. Computational details are available in the ESI.† A total of 780 trajectories were calculated, each taking at least 50 days of CPU time on a 64-bit Linux cluster. gOpenMol[28] was used for trajectory visualization. Analysis of individual trajectories and ensemble averages was done using programs written for these purposes.

IV. Trajectory results and discussion

1. Thermal excitation and dissociation of G·[C–H]$^-$ and G·[C–H]$^-$_PT

100 trajectories were completed for each of G·[C–H]$^-$ and G·[C–H]$^-$_PT which were heated to a vibrational temperature of 960 K. Trajectories were sorted by reaction pathways and dissociation products. Results are collected in Table 1. All dissociation trajectories have base pair center-of-mass (CM) separation exceeding 8 Å and intra-base pair hydrogen bonds dissociating to a distance larger than 4 Å. Error limits for reaction probabilities are the statistical uncertainties calculated on the basis of the numbers of total trajectories, the numbers of dissociation trajectories, and the numbers of PT trajectories under different conditions. For both G·[C–H]$^-$ and G·[C–H]$^-$_PT, the most common trajectory outcome is non-dissociative. Out of the 100 trajectories calculated for G·[C–H]$^-$, only 33 result in dissociation before the termination of the trajectories, of which half dissociate into [G–H]$^-$ + C and the other half into G + [C–H]$^-$. The same dissociation yield and product branching ratios were obtained from the trajectories calculated for G·[C–H]$^-$_PT.

A typical dissociation trajectory is demonstrated in Fig. 3, with the base pair initiated at the G·[C–H]$^-$ conformation. Fig. 3a plots the system potential energy (PE) and the CM distance between guanine and cytosine along the trajectory. Bond lengths plotted in Fig. 3b and c correspond to three intra-base pair hydrogen bonds. Oscillations in the PE and in the bond lengths reflect the vibrations of the base pair and dissociation products, including zero-point energies (ZPEs). In this trajectory, intra-base pair PT through the G(N1)–H1–C(N3) hydrogen bond occurs at 1100 fs, followed by base pair dissociation within $\sim$100 fs. Fig. 3d tracks reactant and product E_{trans} and E_{rot}. Here again, oscillations in E_{trans} and E_{rot} are due to molecular vibrations and inter-molecular motions. The oscillation-averaged E_{trans} remains less than 0.1 eV throughout the trajectory, except that at $\sim$1150 fs when the base pair starts to dissociate, the recoil energy increases to 0.46 eV rapidly so that guanine and cytosine gain sufficient momentum to separate from each other. Base pair loses six vibrational modes in dissociation, of which the stretching of intra-base pair hydrogen bonds becomes the reaction coordinate, and the other five translational modes (corresponding to bending, torsion, sliding and scissoring of the two base units) become intermolecular motions of dissociation products. As a result, the products carry more E_{rot} than the reactant. Base pair separation continues till the end of the trajectory; by then the two moieties are separated by 8 Å.

The most important feature of the thermal excitation trajectories is the PT along G(N1)–H1–C(N3), as demonstrated in Fig. 3b. Among the trajectories originating from G·[C–H]$^-$, 35% have transferred H1 once along G(N1)–H1–C(N3) during the trajectory time, 12% have transferred H1 twice, 14% have transferred H1

Table 1 Trajectory results for thermal excitation of deprotonated G·C at 960 K[a]

	Dissociation (%)		No PT (%)		Single PT (%)		2 × PT (%)		3 × PT (%)		≥4 × PT (%)	
Non-diss.%	[G–H]$^-$ + C	G + [C–H]$^-$	Non-diss.	Diss.	Non-diss.	Diss.	Non-diss.	Diss.	Non-diss.	Diss.	Non-diss.	Diss.
					G·[C–H]$^-$							
67 ± 4	16 ± 3	17 ± 3	21 ± 4	15 ± 3	23 ± 4	12 ± 3	9 ± 3	3 ± 2	11 ± 3	3 ± 2	3 ± 2	0
					G·[C–H]$^-$_PT							
66 ± 4	18 ± 3	16 ± 3	22 ± 4	10 ± 3	17 ± 3	13 ± 3	18 ± 3	5 ± 2	3 ± 2	4 ± 2	6 ± 2	2 ± 1

[a] Probabilities and uncertainties were calculated on the basis of 100 trajectories for each structure.

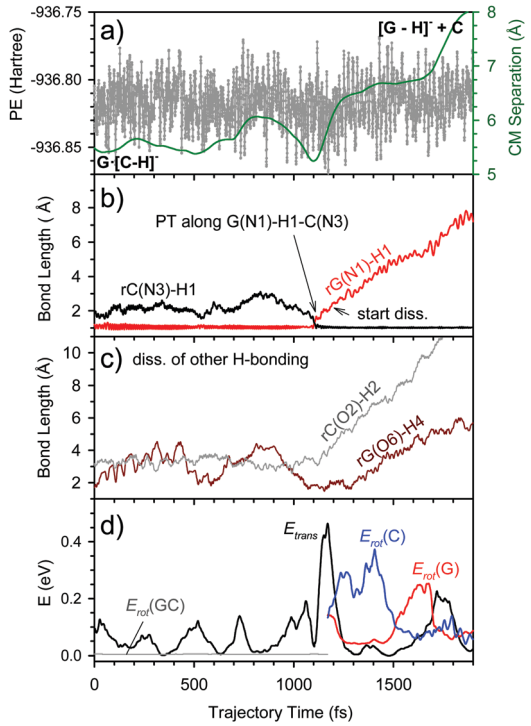

Fig. 3 A representative trajectory for excitation of G·[C–H]$^-$ at 960 K, showing the variations in (a) PE and center-of-mass distance between guanine and cytosine, (b) G(N1)–H1–C(N3) hydrogen bond length and intra-base pair PT, (c) C(O2)–H2 and G(O6)–H4 hydrogen bond lengths, and (d) reactant/product translational and rotational energies during the trajectory. Video for the trajectory is available in the ESI.†

back and forth three times, and the remaining 3% have the H1 back-and-forth movement at least four times. The corresponding percentages are 30, 23, 7 and 8%, respectively, for the trajectories starting at G·[C–H]$^-$_PT. In addition, PT along G(N2)–H2–C(O2) or G(O6)–H4–C(N4) was observed occasionally (1–2%). Multiple intra-base pair PTs have completely scrambled conformations; as a consequence, the two batches of trajectories starting at different conformations have produced identical dissociation yields and product branching ratios, as summarized in Table 1.

Table 2 reports product mean translational ($\langle E_{trans} \rangle$) and rotational ($\langle E_{rot} \rangle$) energies. The limits for $\langle E_{trans} \rangle$ and $\langle E_{rot} \rangle$ are actually the widths (at half-maximum) of energy distributions. Within statistical uncertainties, no differences were observed in the product E_{trans} and E_{rot} between different starting structures or different product channels. In all cases, most of the thermal excitation energy remains in vibrations, and the transfer of excitation to E_{tran} and E_{rot} is insignificant.

2. Dynamics of TS excitation

Barrier excitation trajectories were simulated by sampling the TS's vibrational levels and reaction coordinate energy with Boltzmann distributions at 960 and 1330 K (100 trajectories for each temperature), respectively. This corresponds to trajectories that pass the TS and go randomly towards G·[C–H]$^-$ and G·[C–H]$^-$_PT. As expected, at both excitation temperatures the numbers of trajectories that initially propagate towards G·[C–H]$^-$ and G·[C–H]$^-$_PT are equal (see the first two columns in Table 3). TS re-crossing (*i.e.* intra-base pair PT) occurs extensively in the trajectories. Fig. 4 shows a typical TS trajectory at 1330 K. The trajectory is directed off TS towards G·[C–H]$^-$, then undergoes PT along G(N1)–H1–C(N3) three times. The first PT occurs at 20 fs, followed by the second one at 120 fs and the third at 820 fs, before the trajectory dissociates to [G–H]$^-$ + C at 1450 fs.

The average probability for intra-base pair PT is 72% for the TS at 960 K (4–8% higher than those for G·[C–H]$^-$ and G·[C–H]$^-$_PT at the same temperature), decreasing to 58% at 1330 K. The reduced PT probability at the higher temperature is simply because more trajectories dissociate at earlier times. The average start times for the first PT are 597 fs at 960 K and 363 fs at 1330 K, and the average durations between the first and second PT are 670 fs at 960 K and 558 fs at 1330 K. For comparison, the average start times for the first PT in the 960 K thermal excitation trajectories of G·[C–H]$^-$ and G·[C–H]$^-$_PT are 737 and 770 fs, respectively; and the respective average durations between the first and second PT are 544 and 494 fs. On the other hand, the RRKM predicted PT durations for G·[C–H]$^-$ and G·[C–H]$^-$_PT are 1066 and 1300 fs at 960 K, and 690 and 780 fs at 1330 K, respectively. Therefore, direct dynamics has predicted a much faster PT than statistical modeling, and a significant fraction of PT/TS re-crossing occur within the first 100 fs of the trajectories.

TS excitation yields a higher dissociation probability than the thermal excitation of base pairs. At 960 K, the dissociation yield is 43% for TS *vs.* 33% for G·[C–H]$^-$ and 34% for G·[C–H]$^-$_PT. The product branching between [G–H]$^-$ + C and G + [C–H]$^-$ remains equal following 960 K TS excitation, and there is no dependence of final products on the initial trajectory direction. Of the trajectories initially directed towards G·[C–H]$^-$, the fractions of dissociation into [G–H]$^-$ + C and G + [C–H]$^-$ are 11/51 and 10/51, respectively; for the trajectories

Table 2 Product mean translational and rotational energies in thermal excitation trajectories[a]

		$\langle E_{trans} \rangle$ (eV)		$\langle E_{rot} \rangle$ (eV)	
Starting structure	Temperature (K)	[G–H]$^-$ + C	G + [C–H]$^-$	[G–H]$^-$ + C	G + [C–H]$^-$
G·[C–H]$^-$	960	0.12 ± 0.10	0.08 ± 0.07	0.21 ± 0.12	0.22 ± 0.11
G·[C–H]$^-$_PT	960	0.07 ± 0.06	0.10 ± 0.08	0.21 ± 0.13	0.19 ± 0.12
TS	960	0.09 ± 0.10	0.06 ± 0.06	0.24 ± 0.14	0.24 ± 0.14
	1330	0.08 ± 0.06	0.10 ± 0.07	0.25 ± 0.15	0.28 ± 0.16

[a] Average energies and widths of distributions were calculated on the basis of 100 trajectories for each condition.

Table 3 Trajectory results for TS excitation at different temperatures[a]

Trajectory initially directed towards		Dissociation (%)		Intra-base pair PT (%)				
G·[C–H]$^-$_PT	G·[C–H]$^-$	[G–H]$^-$ + C	G + [C–H]$^-$	no	1×	2×	3×	≥4×
			960 K					
49 ± 5	51 ± 5	22 ± 4	21 ± 4	28 ± 4	33 ± 5	27 ± 4	8 ± 3	4 ± 2
			1330 K					
50 ± 5	50 ± 5	45 ± 5	37 ± 5	42 ± 5	19 ± 4	26 ± 4	5 ± 2	8 ± 3

[a] Probabilities and uncertainties were calculated on the basis of 100 trajectories at each temperature.

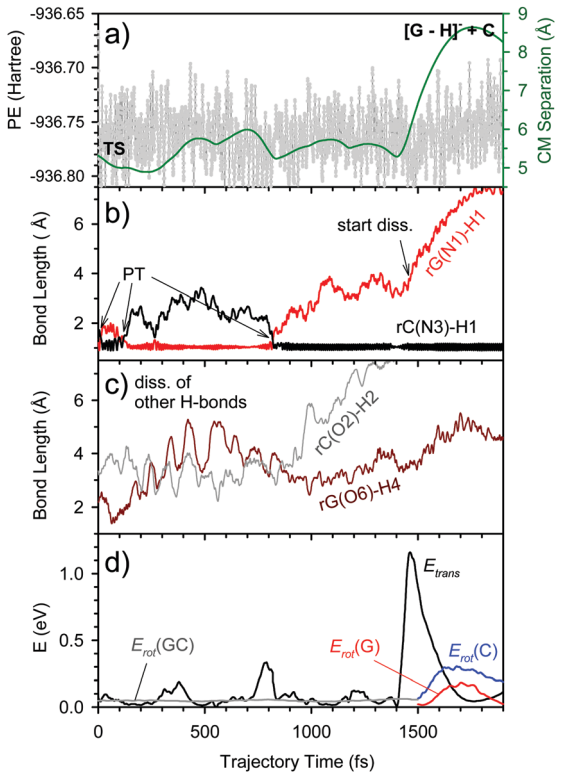

Fig. 4 A representative TS trajectory at 1330 K, showing the variations in (a) PE and center-of-mass distance between guanine and cytosine, (b) G(N1)–H1–C(N3) hydrogen bond length and intra-base pair PT, (c) C(O2)–H2 and G(O6)–H4 hydrogen bond lengths, and (d) reactant/product translational and rotational energies during the trajectory. Video for the trajectory is available in the ESI.†

initially directed towards G·[C–H]$^-$_PT, the corresponding fractions are 11/49 and 11/49, respectively.

When the TS excitation temperature increases to 1330 K, the dissociation yield increases to 82%, and conformation-specific dissociation preference starts emerging. Of the trajectories initially directed towards G·[C–H]$^-$, the fractions of dissociation to [G–H]$^-$ + C and G + [C–H]$^-$ are 16/50 and 29/50, respectively; and of those initially directed towards G·[C–H]$^-$_PT, the fractions of dissociation to [G–H]$^-$ + C and G + [C–H]$^-$ are 29/50 and 8/50, respectively. This implies that with high excitation energy, G·[C–H]$^-$ favors dissociation to G + [C–H]$^-$, whereas G·[C–H]$^-$_PT favors dissociation to [G–H]$^-$ + C. Because the TS has equal chances of going towards G·[C–H]$^-$ and G·[C–H]$^-$_PT, the overall dissociation yield to [G–H]$^-$ + C (45 ± 5%) is only slightly higher than that to G + [C–H]$^-$ (37 ± 5%).

Product energy distributions resulting from TS excitation are included in Table 2, which show no obvious differences from those resulting from the thermal excitation of G·[C–H]$^-$ and G·[C–H]$^-$_PT at the same temperature. When the TS excitation temperature rises from 960 K to 1330 K, product E_{trans} and E_{rot} barely increase. Because the practical trajectory integration time is many orders of magnitude shorter than the realistic situation, the trajectory-calculated dissociation yields may not be directly compared to the experiment or the RRKM predictions. But the pseudo-random sampling procedure used in the trajectory calculations (see the ESI†) has made trajectory-calculated product branching ratios less dependent on trajectory integration time. From that perspective, the TS excitation trajectories at 1330 K indeed predict a modest preference for dissociation into [G–H]$^-$ + C over G + [C–H]$^-$, but not to an extent that is sufficient to justify the strong nonstatistical product branching ratios in the experiment. Apparently there are other factors controlling nonstatistical activation and/or dissociation.

3. CID of G·[C–H]$^-$ and G·[C–H]$^-$_PT

Collisions of deprotonated G·C with Ar were simulated at E_{col} of 3.0 and 5.0 eV. Approximately 100 trajectories were calculated for each combination of the base pair starting structure and E_{col}. All collision trajectories are direct in that there is only one turning point in the relative motion of the centers of mass of G·C and Ar. Trajectories could be grouped into three classes. The first group is non-dissociation collisions resulting in conversion of varying fractions of E_{col} into E_{vib} and E_{rot} of the scattered base pair. Fig. 5a illustrates a typical non-dissociation collision. The set of frames shows the collision time scale, the changes in PE, product recoil energy (E_{recoil}) and E_{rot}, the changes in the CM separations between collision partners and between guanine and cytosine, and the changes in the hydrogen bond lengths and the torsion angle of the G·C plane throughout the trajectory. In this trajectory, the time during which Ar and G·C are interacting strongly is 120 fs (highlighted by the yellow-shaded area). At the instant of collision, the repulsive potential converts a fraction of E_{col} to a combination of PE (as indicated by the spike beginning at 80 fs, shown in the top frame), E_{vib} and E_{rot}. As a result, translational energy drops from the initial 3 eV of E_{col} to 1.3 eV of E_{recoil}. As the reactants separate, some of the PE is converted back to E_{recoil}. After the collision, the base pair goes through multiple PTs along G(N1)–H1–C(N3).

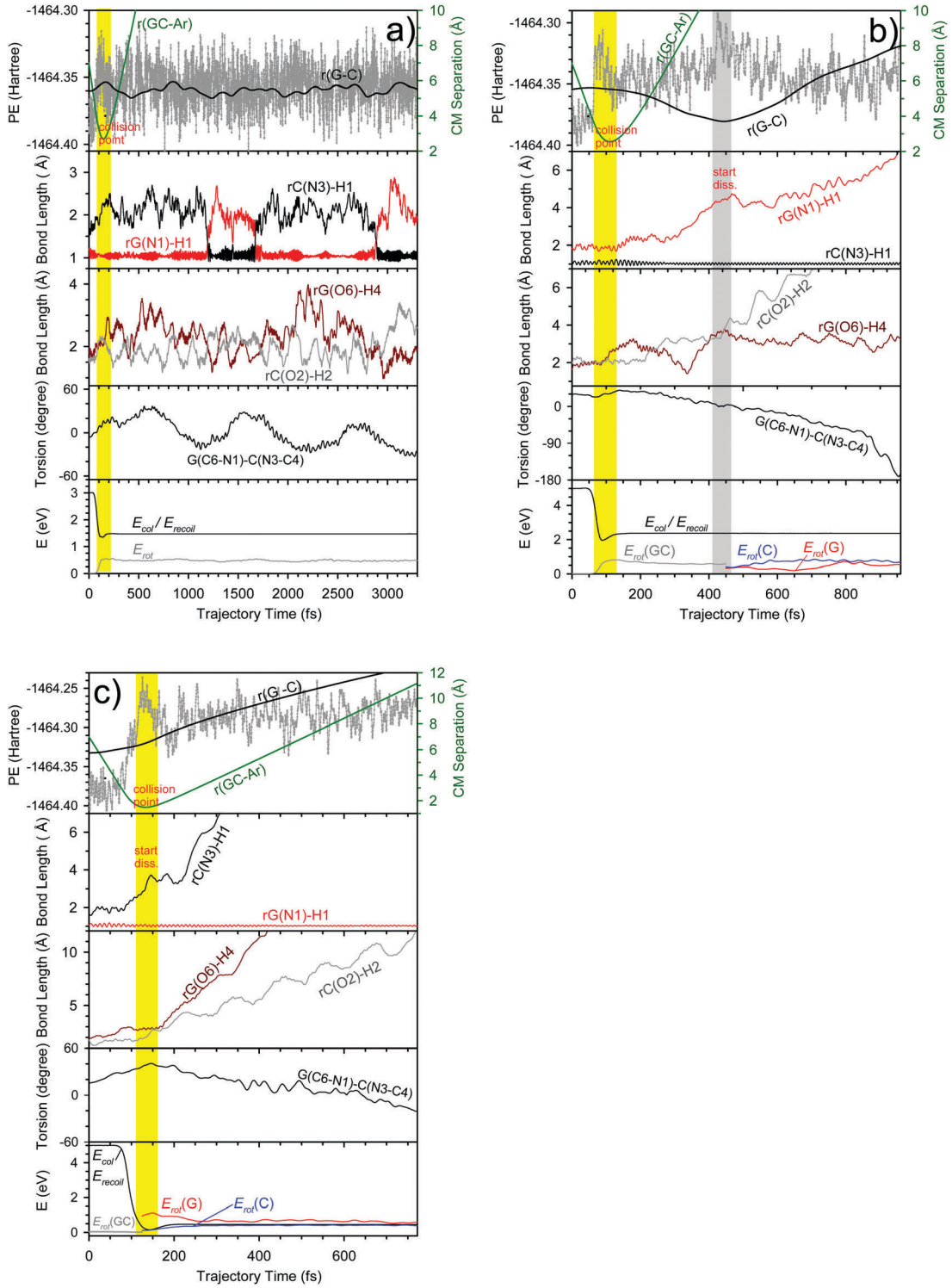

Fig. 5 (a) Non-dissociation collision of G·[C−H]$^-$ with Ar at E_{col} = 3.0 eV, (b) sequential activation and dissociation of G·[C−H]$^-$_PT in collision with Ar at E_{col} = 5.0 eV, and (c) direct, concerted dissociation of G·[C−H]$^-$ in collision with Ar at E_{col} = 5.0 eV. Each set, from the top frame, shows the changes of PE and the CM distances between Ar and G·C and between the two base units, the variations of hydrogen bond lengths and accompanying intra-base pair PT, the twisting of base pair plane, and the changes of reactant/product translational and rotational energies. Videos for the trajectories are available in the ESI.†

The second (also the most common) group of trajectories belongs to sequential "collisional activation – dissociation" with an example depicted in Fig. 5b. The time scale of the collision is arbitrary, but two numbers are relevant: the time between the trajectory start and the onset of strong intermolecular interaction (yellow-shaded area) is 70 fs, and that between

the collision point and the point when the base pair starts to dissociate (gray-shaded area) is 300 fs. In addition to the abrupt changes in various CM separations and bond lengths, collision and dissociation are accompanied by the increase of PE.

The last group could be characterized by ''direct, concerted dissociation'' or shattering.[29] As demonstrated in Fig. 5c, Ar impacts the base pair at 100 fs and the base pair starts to dissociate within a short duration while the Ar atom is still in close proximity. Direct, concerted dissociation was occasionally observed. Only 4% of collisions lead to direct, concerted dissociation at E_{col} = 3.0 eV, increasing to 6% at 5.0 eV, most of which occur at the G·[C–H]$^-$ conformation.

In the experiment, the time between collision and product ion detection ranged up to $\sim 10^2$ μs, which is far longer than the time that is feasible to integrate trajectories. Trajectories were terminated at large CM separations between the two collision partners, thus the partitioning of E_{col} into E_{recoil}, E_{rot} and E_{vib} is known. For small molecules, whether or not the molecule would dissociate could be simply determined by the amount of translational-to-vibrational energy transfer ($T \rightarrow E_{vib}$).[19,30] Trajectories that have $T \rightarrow E_{vib}$ greater than thermal dissociation threshold E_0 are expected to dissociate ultimately if they are integrated for a sufficiently long time. This prescription for sorting dissociation trajectories minimizes the problems arising from shorter simulation times. However, this method may not be completely appropriate for large molecules because of kinetic shifts. CID yields reported in Table 4 are thus based on the numbers of sequential and direct dissociations that have completed during the trajectory times, as judged by the CM separation between the two base units (>8 Å) and the lengths of the intra-base pair hydrogen bonds (>4 Å). The group of trajectories that meet the criterion of ($T \rightarrow E_{vib}$) ≥ E_0 but have not dissociated during the trajectories was analyzed separately and will be discussed below.

It turns out that both dissociation yields and product branching ratios are influenced by the starting structures of the base pair. The dissociation yield of G·[C–H]$^-$ is smaller than that of G·[C–H]$^-$_PT by 3% at E_{col} = 3.0 eV, and by 21% at 5.0 eV. The formation of G + [C–H]$^-$ is favored in the CID of G·[C–H]$^-$, with the product branching ratio $\frac{[G-H]^- + C}{G + [C-H]^-} = \frac{1}{2.1}$ at E_{col} = 3.0 eV and $\frac{1}{2.8}$ at 5.0 eV. An even more strong but opposite preference was observed in the CID of G·[C–H]$^-$_PT, with $\frac{[G-H]^- + C}{G + [C-H]^-} = \frac{6.8}{1}$ at E_{col} = 3.0 eV and $\frac{9}{1}$ at 5.0 eV. The best test for the collision trajectories is to compare with the experiment. The trajectory CID branching ratios for G·[C–H]$^-$ ⇌ G·[C–H]$^-$_PT were calculated on the basis of relative populations of G·[C–H]$^-$ and G·[C–H]$^-$_PT at the experimental temperature and respective trajectory branching ratios for each conformer. The ensemble-averaged results are listed in the last column of Table 4. That is $\frac{[G-H]^- + C}{G + [C-H]^-} = \frac{3.1}{1}$ at E_{col} = 3.0 eV and $\frac{3.4}{1}$ at 5.0 eV. For comparison, the experimental $\frac{[G-H]^- + C}{G + [C-H]^-}$ (taken from CID of deprotonated 9MG·C) is $\frac{6}{1}$ at $E_{col} \geq$ 3.0 eV, while the RRKM value is $\frac{1}{2.7}$ at E_{col} = 3.0 eV and $\frac{1}{4.2}$ at 5.0 eV. Therefore, CID trajectories are in good agreement with the experiment.

In addition to the correct prediction of the dominating CID channel for G·[C–H]$^-$ ⇌ G·[C–H]$^-$_PT, trajectories have reproduced the trend of reaching a nearly energy-independent product branching ratio at high E_{col}. The difference between the absolute values of trajectory and experimental branching ratios could be attributed to the mixing of inaccuracies in the B3LYP/6-31G* interaction potential, replacing the softer Xe atom with Ar, the small batch of trajectories, the limited trajectory integration times, and sampling only head-on collisions at zero impact parameter (see the ESI†). No matter what has caused the discrepancies in absolute product branching ratios, the fact that trajectories have qualitatively reproduced the CID experiment suggests that trajectories have captured the physics necessary to mimic the non-statistical behaviors of the deprotonated G·C base pair.

4. Energy partitioning and kinetic shifts in collisional activation

CID trajectories have predicted a higher dissociation yield for G·[C–H]$^-$_PT and a nonstatistical CID branching ratio for the G·[C–H]$^-$ ⇌ G·[C–H]$^-$_PT ensemble, but a mechanism is needed to explain the underlying reason. To this end, it is useful to first compare the similarities and differences between thermal excitation and collisional activation, and between collisional activation of different base pair conformers. In the thermal excitation of base pairs and the TS, vibrational modes and reaction coordinate energy were sampled at temperatures of 960 and 1330 K, and their average total excitation energies (above ZPE) are equal to collision energies of 3.0 and 5.0 eV, respectively. However, their excitation efficiencies are different.

Table 4 Dissociation yields and product branching ratios in collisions of deprotonated G·C with Ar[a]

Starting structure	E_{col} (eV)	Dissociation %		No PT (%)		PT (%)		Ensemble ave. $\frac{[G-H]^- + C}{G + [C-H]^-}$
		[G–H]$^-$ + C	G + [C–H]$^-$	Non-diss.	Diss.	Non-diss.	Diss.	
G·[C–H]$^-$	3.0	9 ± 3	19 ± 4	39 ± 5	20 ± 4	33 ± 5	8 ± 3	3.1 : 1
G·[C–H]$^-$_PT		27 ± 5	4 ± 2	50 ± 6	27 ± 5	18 ± 4	4 ± 2	
G·[C–H]$^-$	5.0	18 ± 4	51 ± 6	23 ± 4	55 ± 6	8 ± 3	14 ± 4	3.4 : 1
G·[C–H]$^-$_PT		81 ± 4	9 ± 3	6 ± 2	80 ± 4	4 ± 2	10 ± 3	

[a] Probabilities and uncertainties were calculated on the basis of ~100 trajectories for each condition.

Table 5 Efficiencies for translational-to-internal energy transfer and product mean translational and rotational energy in collisions of deprotonated G·C with Ar[a]

		$\langle T \rightarrow E_{int}$ %$\rangle$				$\langle E_{trans}\rangle$ (eV)		$\langle E_{rot}\rangle$ (eV)	
Starting structure	E_{col} (eV)	All	No diss.	$[G–H]^-$ + C	G + $[C–H]^-$	$[G–H]^-$ + C	G + $[C–H]^-$	$[G–H]^-$ + C	G + $[C–H]^-$
G·$[C–H]^-$	3.0	56 ± 16	50 ± 13	71 ± 9	73 ± 8	1.02 ± 0.25	1.04 ± 0.28	0.30 ± 0.12	0.34 ± 0.19
G·$[C–H]^-$_PT		56 ± 15	49 ± 13	71 ± 8	69 ± 5	1.04 ± 0.25	1.11 ± 0.24	0.38 ± 0.19	0.43 ± 0.27
G·$[C–H]^-$	5.0	58 ± 15	47 ± 15	64 ± 13	63 ± 17	2.01 ± 0.71	2.09 ± 0.72	0.66 ± 0.34	0.67 ± 0.40
G·$[C–H]^-$_PT		59 ± 16	33 ± 5	61 ± 13	65 ± 17	2.17 ± 0.69	1.98 ± 0.88	0.61 ± 0.32	0.50 ± 0.25

[a] Averages and widths of distributions were calculated on the basis of ~100 trajectories for each condition.

As revealed by the data in Table 2, the fraction of the excitation energy partitioned into E_{tran} and E_{rot} is less than 8% in thermal excitation. Most of the excitation is randomly distributed over vibrational modes and reaction coordinates. This is clearly not the case in collisional activation. Table 5 compares the efficiencies of $T \rightarrow E_{in}$(internal energy)$\%\left(=\frac{E_{col}-E_{recoil}}{E_{col}}\%\right)$, and product $\langle E_{recoil}\rangle$ and $\langle E_{rot}\rangle$ in the collision trajectories. Data were averaged over all trajectories (including dissociation and non-dissociation) and over individual product channels, respectively. At both collision energies, the batches (counting all trajectories) of G·$[C–H]^-$ and G·$[C–H]^-$_PT result in nearly identical $\langle T \rightarrow E_{int}\%\rangle$, *i.e.* 56% at E_{col} = 3.0 eV and 58–59% at 5.0 eV. Similar efficiencies for $T \rightarrow E_{int}$ were observed when comparing the same product channels resulting from CID of G·$[C–H]^-$ and G·$[C–H]^-$_PT, respectively.

Energy partitioning may be better visualized by plotting binned probability distributions for $T \rightarrow E_{rot}$ and $T \rightarrow E_{vib}$, the latter of which was calculated by subtracting $T \rightarrow E_{rot}$ from $T \rightarrow E_{int}$. The top row of Fig. 6 summarizes the results for all trajectories including dissociation and non-dissociation. For G·$[C–H]^-$, $T \rightarrow E_{vib}$ ranges from 0.2 to 2.6 eV (with an average of 1.40 eV) at E_{col} = 3.0 eV and from 0.4 to 4.4 eV (average 2.38 eV) at E_{col} = 5.0 eV; while for G·$[C–H]^-$_PT, $T \rightarrow E_{vib}$ ranges from

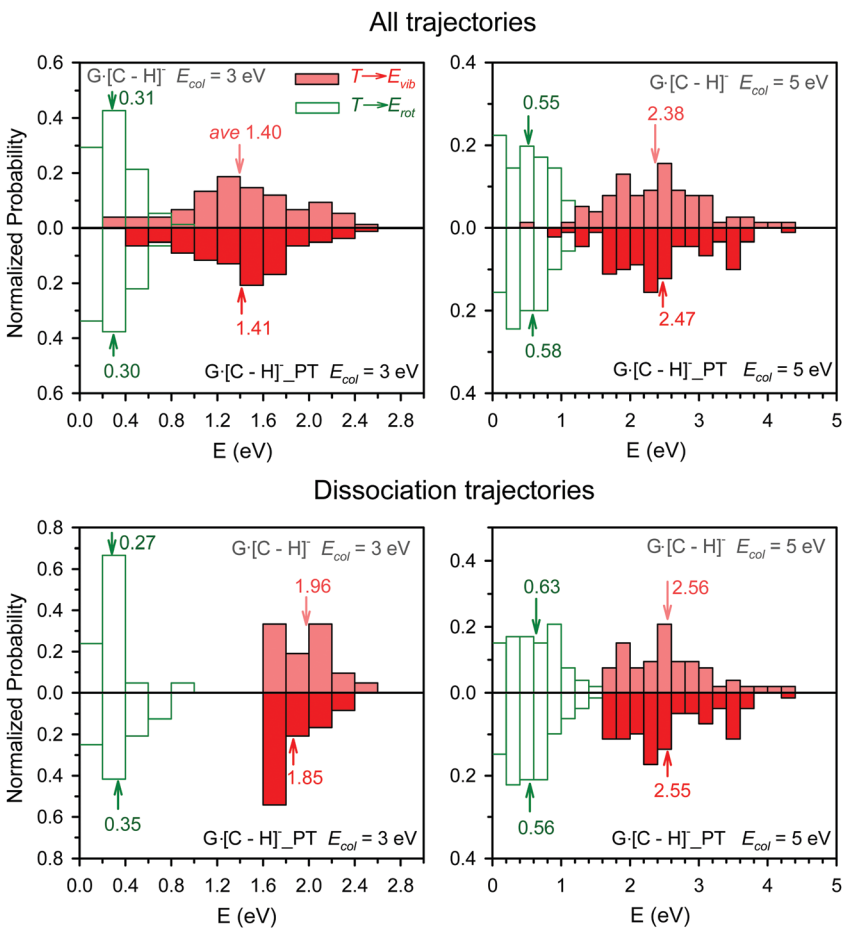

Fig. 6 Distribution plots for translational-to-vibrational and translational-to-rotational energy transfer. Bin size is 0.2 eV. Arrows indicate average values.

Table 6 Results of the trajectories that meet the dissociation energy requirement but have not dissociated[a]

Starting structure	E_{col} (eV)	Probability (%)			$\langle T \rightarrow E_{rot} \rangle$ (eV)	$\langle T \rightarrow E_{vib} \rangle$ (eV)
		Total	No PT	PT		
G·[C–H]$^-$	3.0	5 ± 2	4 ± 2	1 ± 1	0.26	1.94
G·[C–H]$^-$_PT		3 ± 2	3 ± 2	0	0.13	2.38
G·[C–H]$^-$	5.0	20 ± 4	17 ± 4	3 ± 2	0.37	2.42
G·[C–H]$^-$_PT		1 ± 1	0	1 ± 1	0.24	1.69

[a] Probabilities, averages and uncertainties were calculated on the basis of ~100 trajectories for each condition.

0.4 to 2.6 eV (average 1.41 eV) at E_{col} = 3.0 eV and from 0.8 to 4.4 eV (average 2.47 eV) at 5.0 eV. The bottom row of Fig. 6 compares the dissociation trajectories only. The dissociation of G·[C–H]$^-$_PT yields the same or slightly lower $\langle T \rightarrow E_{vib} \rangle$ compared to that of G·[C–H]$^-$. Distributions of $T \rightarrow E_{rot}$ and their averages are also presented in Fig. 6. The amount of energy partitioned into E_{rot} never exceeds 1.0 eV at E_{col} = 3.0 eV or 1.6 eV at E_{col} = 5.0 eV.

Without the analysis of product energy partitioning, conformation-specific CID would have been thought to arise from the different $T \rightarrow E_{vib}$ efficiencies for G·[C–H]$^-$ *vs.* G·[C–H]$^-$_PT. The fact that G·[C–H]$^-$ and G·[C–H]$^-$_PT present nearly identical $T \rightarrow E_{vib}$ distributions for all product channels and at all E_{col} in essence tells that this is not the determining factor. Average values of $T \rightarrow E_{rot}$ were also evaluated for different conformers, that is 0.31 eV for G·[C–H]$^-$ *vs.* 0.30 eV for G·[C–H]$^-$_PT at E_{col} = 3.0 eV, and 0.55 eV for G·[C–H]$^-$ *vs.* 0.58 eV for G·[C–H]$^-$_PT at E_{col} = 5.0 eV. The differences between $T \rightarrow E_{rot}$ for different conformers are too small to cause conformation-specific effects in CID. In principle, the contribution of base pair rotational energy to dissociation should also be considered. However, the conservation of angular momentum dictates that most of the rotational energy must stay on rotation during the dissociation, and thus is unavailable to drive dissociation.

As rationalized above, the analysis of dissociation collisions does not include the trajectories that meet the dissociation energy requirement but have maintained the base-pair structure within the 4 ps trajectory time. The yields and energy partitioning for these collisions are summarized in Table 6. Such collisions are most significant in the trajectories of G·[C–H]$^-$. At E_{col} = 5.0 eV, 20% of G·[C–H]$^-$ transfer enough energy to vibrations but have not dissociated, of which 85% have maintained the original conformation throughout the trajectories; under the same conditions, only ≤3% of G·[C–H]$^-$_PT have run into such collisions. If assigning these trajectories to dissociation product channels randomly on the basis of the thermal excitation trajectory results, the ensemble-averaged $\frac{[G-H]^- + C}{G + [C-H]^-}$ becomes $\frac{2.6}{1}$ at E_{col} = 3.0 eV and $\frac{3.1}{1}$ at 5.0 eV. The preference for [G–H]$^-$ + C is then weakened by 10–20%. This implies that the nonstatistical CID product preference is partially resulting from the group of G·[C–H]$^-$ collisions that present significant kinetic shifts and might not dissociate within the time frame of the mass spectrometry experiment.

Finally, collision trajectories live the early stage before thermal equilibrium is attained, and molecules are excited with non-random, localized vibrational energies. This is reflected by the fact that the collision trajectories experience much less intra-base pair PT than the thermal excitation trajectories at the equivalent energy, *i.e.* 41% and 23% for collisionally activated G·[C–H]$^-$ and G·[C–H]$^-$_PT at E_{col} = 3.0 eV *vs.* 64% for G·[C–H]$^-$, 68% for G·[C–H]$^-$_PT and 72% for the TS at 960 K. An even lower PT probability (14–22%) was found for the collision trajectories at E_{col} = 5.0 eV. A dynamics consequence of the different PT probabilities is that the thermal excitation trajectories have scrambled initial conformations; whereas the collision trajectories are not able to sample different conformations sufficiently, and most of the collisionally activated base pairs have therefore remained at their starting conformations at the dissociation point.

V. Conclusions

Direct dynamics trajectory simulations were performed at the B3LYP/6-31G* level of theory to reveal the reaction dynamics of deprotonated G·C base pairs and their TS under thermal excitation and collisional activation. Analysis of trajectories indicates that, regardless of initial conditions (*i.e.*, starting base pair structures, relative populations, and temperatures), thermally excited base pairs and TS dissociate into [G–H]$^-$ + C and G + [C–H]$^-$ equally. In contrast, collisional activation results in a strong preference for dissociation of the (G·[C–H]$^-$ ⇌ G·[C–H]$^-$_PT) ensemble into [G – H]$^-$ + C, reproducing the nonstatistical product branching reported in the CID experiment. Some of the factors which control the nonstatistical CID are beginning to be understood, which include: (1) few intra-base pair proton transfer in collisions renders conformation scrambling less likely. Most of the base pairs have therefore maintained their starting conformations upon dissociation; and (2) the G·[C–H]$^-$_PT conformer dissociates more quickly than G·[C–H]$^-$, and thus presents a higher dissociation probability in trajectory simulations and likely within the mass spectrometric detection time window in the experiment, albeit that the two conformers have similar $T \rightarrow E_{vib}$ efficiencies. Work will continue to pinpoint other factors controlling the dissociation of deprotonated G·C.

Conflicts of interest

There are no conflicts to declare.

Acknowledgements

This work was supported by the National Science Foundation Award (Grant No. CHE-1464171) and Queens College Research Enhancement Award. The author thanks William Hase (Texas Tech) and his group for providing assistance with the applications of Venus, and Seogjoo Jang (CUNY Queens College) for helpful discussion.

References

1 B. Boudaiffa, P. Cloutier, D. Hunting, M. A. Huels and L. Sanche, *Science*, 2000, **287**, 1658–1660.
2 H. Abdoul-Carime, S. Gohlke and E. Illenberger, *Phys. Rev. Lett.*, 2004, **92**, 168103.
3 S. Denifl, S. Ptasińska, M. Probst, J. Hrušák, P. Scheier and T. D. Märk, *J. Phys. Chem. A*, 2004, **108**, 6562–6569.
4 W. Lu, H. Teng and J. Liu, *Phys. Chem. Chem. Phys.*, 2016, **18**, 15223–15234.
5 R. R. Sinden, C. E. Pearson, V. N. Potaman and D. W. Ussery, *Adv. Genome Biol.*, 1998, **5A**, 1–141.
6 L. Sun, Y. Bu, Q. Qiao, Q. Liu and Z. Guo, *Comput. Theor. Chem.*, 2012, **980**, 23–31.
7 W. Lu and J. Liu, *Phys. Chem. Chem. Phys.*, 2016, **18**, 32222–32237.
8 U. Dornberger, M. Leijon and H. Fritzsche, *J. Biol. Chem.*, 1999, **274**, 6957–6962.
9 A. M. Ababneh, C. C. Large and S. Georghiou, *Biophys. J.*, 2003, **85**, 1111–1127.
10 M. C. Lind, P. P. Bera, N. A. Richardson, S. E. Wheeler and H. F. Schaefer, III, *Proc. Natl. Acad. Sci. U. S. A.*, 2006, **103**, 7554–7559.
11 R. D. Levine and R. B. Bernstein, *Molecular Reaction Dynamics and Chemical Reactivity*, Oxford University Press, New York, 1987.
12 P. B. Armentrout, *Int. J. Mass Spectrom.*, 2000, **200**, 219–241.
13 J. Liu, B. Van Devener and S. L. Anderson, *J. Chem. Phys.*, 2002, **116**, 5530–5543.
14 R. A. Marcus, *J. Chem. Phys.*, 1952, **20**, 359–364.
15 M. B. More, E. D. Glendening, D. Ray, D. Feller and P. B. Armentrout, *J. Phys. Chem.*, 1996, **100**, 1605–1614.
16 W. L. Hase, *Acc. Chem. Res.*, 1983, **16**, 258–264.
17 D. L. Bunker and W. L. Hase, *J. Chem. Phys.*, 1973, **59**, 4621–4632.
18 P. T. Fenn, Y. J. Chen, S. Stimson and C. Y. Ng, *J. Phys. Chem. A*, 1997, **101**, 6513–6522.
19 J. Liu, K. Song, W. L. Hase and S. L. Anderson, *J. Chem. Phys.*, 2003, **119**, 3040–3050.
20 E. Martínez-Núñez, S. A. Vázquez, F. J. Aoiz and J. F. Castillo, *J. Phys. Chem. A*, 2006, **110**, 1225–1231.
21 Z. Homayoon, S. Pratihar, E. Dratz, R. Snider, R. Spezia, G. L. Barnes, V. Macaluso, A. Martin Somer and W. L. Hase, *J. Phys. Chem. A*, 2016, **120**, 8211–8227.
22 B. H. Munk, C. J. Burrows and H. B. Schlegel, *Chem. Res. Toxicol.*, 2007, **20**, 432–444.
23 X. Hu, W. L. Hase and T. Pirraglia, *J. Comput. Chem.*, 1991, **12**, 1014–1024.
24 W. L. Hase, K. Bolton, P. de Sainte Claire, R. J. Duchovic, X. Hu, A. Komornicki, G. Li, K. Lim, D. Lu, G. H. Peslherbe, K. Song, K. N. Swamy, S. R. Vande Linde, A. Varandas, H. Wang and R. J. Wolf, *VENUS 99: A General Chemical Dynamics Computer Program*, Texas Tech Univeristy Lubbock, TX, 1999.
25 V. Bakken, J. M. Millam and H. B. Schlegel, *J. Chem. Phys.*, 1999, **111**, 8773–8777.
26 M. J. Frisch, G. W. Trucks, H. B. Schlegel, G. E. Scuseria, M. A. Robb, J. R. Cheeseman, G. Scalmani, V. Barone, B. Mennucci, G. A. Petersson, H. Nakatsuji, M. Caricato, X. Li, H. P. Hratchian, A. F. Izmaylov, J. Bloino, G. Zheng, J. L. Sonnenberg, M. Hada, M. Ehara, K. Toyota, R. Fukuda, J. Hasegawa, M. Ishida, T. Nakajima, Y. Honda, O. Kitao, H. Nakai, T. Vreven, J. J. A. Montgomery, J. E. Peralta, F. Ogliaro, M. Bearpark, J. J. Heyd, E. Brothers, K. N. Kudin, V. N. Staroverov, T. Keith, R. Kobayashi, J. Normand, K. Raghavachari, A. Rendell, J. C. Burant, S. S. Iyengar, J. Tomasi, M. Cossi, N. Rega, J. M. Millam, M. Klene, J. E. Knox, J. B. Cross, V. Bakken, C. Adamo, J. Jaramillo, R. Gomperts, R. E. Stratmann, O. Yazyev, A. J. Austin, R. Cammi, C. Pomelli, J. W. Ochterski, R. L. Martin, K. Morokuma, V. G. Zakrzewski, G. A. Voth, P. Salvador, J. J. Dannenberg, S. Dapprich, A. D. Daniels, O. Farkas, J. B. Foresman, J. V. Ortiz, J. Cioslowski and D. J. Fox, *Gaussian 09, Revision D.01*, Gaussian, Inc., Wallingford, CT, 2013.
27 G. B. Bacskay, *Chem. Phys.*, 1981, **61**, 385–404.
28 L. Laaksonen, gOpenMol, Center for Scientific Computing, Espoo, Finland, 3.0 edn., 2005, available at www.csc.fi/gopenmol/.
29 S. O. Meroueh, Y. Wang and W. L. Hase, *J. Phys. Chem. A*, 2002, **106**, 9983–9992.
30 J. Liu, B. Uselman, J. Boyle and S. L. Anderson, *J. Chem. Phys.*, 2006, **125**, 133115.

